J Mater Sci (2020) 55:4005–4016

Energy materials

An effective photocatalytic and photoelectrochemical performance of β/γ-MnS/CdS composite photocatalyst for degradation of flumequine and oxytetracycline antibiotics under visible light irradiation

Ali İmran Vaizoğullar[1,*]

[1] *Vocational School of Health Care, Medical Laboratory Programme, Muğla Sıtkı Koçman University, 48000 Muğla, Turkey*

Received: 4 October 2019
Accepted: 9 December 2019
Published online: 13 December 2019

ABSTRACT

Herein, we report the MnS, CdS and MnS/CdS nanoparticles prepared by precipitation method. The as-synthesized particles were characterized using by scanning electron microscope, X-ray diffraction, UV-diffuse reflectance spectroscopy, photoluminescence, X-ray photoelectron spectroscopy and photoelectrochemical technique. MnS/CdS composite combination enhanced the optical, photocatalytic, and photoelectronic properties of the samples. Photocatalytic performances of the samples were evaluated under visible light irradiation. The photoelectrode activity of all samples was also investigated. MnS/CdS composites were found as efficient photocatalysts under visible light. The enhanced photocatalysis of the composites was attributed to the possible defect structure, high electron density of CdS and inhibition of electron/hole pairs as well as optimal content of CdS in the composite system. MnS/CdS composites must be evaluated for photocatalytic and photoelectrochemical activities with broader visible light range.

Introduction

Environmental pollution and energy shortage are major problems of the modern world [1, 2]. To overcome these problems, many researchers are working on green energy and green chemistry [3]. Partially metabolized antibiotics are creating serious environmental problem as they are being detected in ground water, sediment, etc. In addition, they intervene in the growth of living cells and lead to the proliferation of antibiotic-resistant microorganisms [4]. Tetracycline (TC) has been found in aquatic environments that negatively affected the environment itself as well as human, animals' health [2]. Fluoroquinolones (FQs) are widely used as broad-spectrum antibiotics, which are commonly found in ground or fresh water (approx. 2.5–50 ng L^{-1}) [5]. Antibiotics cause allergies, toxicity, and can lead to the antibiotic-resistant bacteria in the environment. Adsorption, biodegradation, filtration, semiconductor photocatalysts, etc., have been applied

Address correspondence to E-mail: aliimran@mu.edu.tr

https://doi.org/10.1007/s10853-019-04299-6

to eliminate such antibiotics from waste water. Semiconductor composites are widely used to remove organic contaminants [6]. Photocatalysts are ideal materials to convert solar energy into be electrochemical energy. This process degrades organic pollutant and produces H_2 that is a green energy [7]. Semiconductor composites are efficient absorber due to their multi-functional properties such as high absorption coefficients, plasmonic effects, electron injection and wider absorption bands. [8, 9]. Semiconductors catalyze in photoelectric events that fabricate induced electrons and holes under UV–visible irradiation. These charge carriers can start chemical reaction on the catalysts surface [10]. The efficiency of the photocatalytic activity of pristine semiconductors has been increased making their composites that increase the light absorption and separation of charge carries [11].

The use of metal sulfides (MS) is trending due to special crystal and energy band structure. It is being used as a substitute for noble metals in the modification of CdS [12]. MnS is a perfect energy storage material but carries certain disadvantages in photocatalytic and photoelectrochemical applications [13]. Coupled structure with other semiconductors such as CdS, TiO_2, and MoS_2 can be made to overcome their deficiencies. A contact-type complex consisting of different bandgaps can exhibit a different structure in electric field. This case helps to increase the separation of electron to hole (e^-/h^+) pairs [14]. Consequently, the energy levels of the two semiconductors can come to equilibrium to act as a staggered heterojunction. Although the photocatalytic activity of a photocatalyst has been significantly enhanced compared with each bare photocatalyst, charge migration rate, separation efficiency of the electron and hole (e^-/h^+) pairs, absorption in visible region and available active sites of photocatalysts still need to be improved. CdS is a II–IV promising semiconductor photocatalysis. CdS has high photocatalytic activity and wider visible light absorption spectra with narrow band gap ($\sim$ 2.2 eV) [15]. However, the oxidation of photogenerated holes, which causes photocorrosion of CdS, results in poor stability in aqueous solutions [16].

Different methods have been applied to increase the photocatalytic performance of CdS. It has been synthesized as a core shell structure to enhance the flow charge carrier and inhibit charge recombination. It can also be modified as co-catalysts onto the semiconductors [17]. This limits the charge recombination and increases the charge separation by facilitating energy band bending and reveals a new electric field [18]. Until now, there are limited studies with MnS/CdS composites and their degradation studies. Yang et al. [19] prepared ZnO/TiO_2/CdS composites with enhanced photoelectrocatalytic performance. Wang et al. [20] studied MoS_2-modified $Mn_{0.2}Cd_{0.8}S$/MnS heterojunction while Li et al. [21] synthesized $Mn_xCd_{1-x}S$ photocatalyst, both for enhanced photocatalytic H_2 evolution.

Herein, we report a new composite MnS/CdS photocatalyst fabricated through a facile precipitation method. The photocatalytic and photoelectrochemical performances of composites were tested under visible light irradiation with different molar ratios of CdS. The as-prepared MnS/CdS heterojunctions presented a significantly enhanced photocatalytic and photoelectrochemical activity.

Experimental

Synthesize of MnS, CdS and MnS/CdS composites

To synthesize the CdS nanomaterials (NM), a facile chemical precipitation method was used. Initially, 0.63 g NaS was dissolved in methanol/water mixture (20/80 v/v) and 1 mL of ethylene glycol was added into it. The mixture was stirred for 2 h (Solution A). 0.56 g of $Cd(NO_3)_2$ was dissolved in 40 mL of water, added into solution A and stirred for 2 h. The obtained precipitate was filtered, centrifuged for 30 min, and dried in an oven at 80 °C for 3 h that revealed CdS NM.

The same method was used to synthesize MnS NM. Around 0.84 g of NaS was dissolved in methanol/water mixture (20/80 v/v), and 1 mL of ethylene glycol was added into it. The mixture was stirred for 2 h (Solution B). 1.12 g of $Mn(NO_3)_2$ was dissolved in 50 mL of water and dropped to Solution B. The MnS particles were filtered and centrifuged for 30 min. The obtained MnS sample was dried at 90 °C for 2 h before calcination at 200 °C.

MnS/CdS composite materials were prepared by precipitation CdS in MnS solution. In this process, 0.5 g of MnS particles was mixed with relative $Cd(NO_3)_2$ and NaS components in 100 mL of methanol/water (20/80 v/v) solution. The mixture was stirred for 3 h. The obtained samples with

various MnS/CdS molar ratio (1/3.5), (1/5) and (1/7) were labeled as MC1, MC2 and MC3, respectively.

Characterization

The crystalline structures were examined by X-ray diffraction (XRD: Rigaku D/MAX 350) using copper K radiation (k = 0.154056 nm). The microstructure and shape of the particles were investigated using scanning electron microscope (SEM) (JEOL JSM-7600F). X-ray photoelectron spectroscopic (XPS) measurement was taken using a PHI 5000 Versa Probe. The photoluminescence (PL) emission spectra of the samples were obtained using a spectrofluorometric (Spex 500 M, USA). The UV–Vis DRS analyses of all the samples were performed using a Lambda 35 UV–Vis spectrophotometer in the solid state. Raman studies were performed at room temperature using Raman spectrophotometer (Bruker IFS 66/S, FRA 106/S, HYPERION 1000, RAMANSCOPE II). The recorded spectra were obtained using 532 nm laser. The electrochemical impedance spectra (EIS) were analyzed on an impedance analyzer (Gamry Potentiostat/Galvanostat/ZRA Reference 3000) using a standard three-electrode system with the samples as the working electrodes, a saturated calomel electrode (SCE) as the reference electrode, and a Pt wire as the counter electrode. Frequency operating range was specified as 1 kHz–10^7 Hz.

Photocatalytic performance studies

The photocatalytic performance of the as-synthesized catalysts was evaluated by decomposition of the Oxytetracycline (OTC) and flumequine (FLQ) antibiotics under visible light irradiation. A special photoreactor was used to reveal the degradation experiments. 300 W Xenon arc lamp was used as visible light source. 0.1 g of samples was dispersed in a 50 mL FLQ (10 ppm) and OTC (10 ppm) solution. Natural pH was maintained throughout the catalytic reactions. The FLQ and OTC solutions were stirred for 1 h to adjust adsorption/desorption equilibrium. After that, 2 mL aliquot was taken and filtered to measure absorbance in UV–Vis spectrophotometer. The residual FLQ and OTC concentration was estimated using Eq. 1 as given below:

$$\%\text{Degradation} = \frac{C_0 - C}{C_0} \times 100 = \frac{A_0 - A_t}{A_t} \times 100 \qquad (1)$$

where A_0 and A_t are the initial and final absorbencies of FLQ at 248 nm and OTC at 251 nm.

According to the Beer–Lambert law, initial and final absorbencies represent the initial C_0 and final C concentrations of the FLQ and OTC antibiotics.

XRD analysis

The structural properties of the prepared MnS, CdS and MnS/CdS composites were determined by X-ray diffraction. The (1 1 1) peak at 27.5 in Fig. 1a shows meta-stable β-MnS phase (Cubic phase). Peaks at 25.61°, 31.2° and 51.01° can be indexed to (1 0 0), (1 0 1) and (1 0 3) planes of γ-MnS phases [22]. Two different phases were obtained in this preparation method. During the formation of the MnS structures, probably β-MnS phase has minimal free energy closely followed by that of γ-phase [23]. This means β-MnS and γ-MnS have not transformed to α-MnS at 200 °C of calcination temperature. The most intense peak was obtained at 31.2°. It is possible that the preferential growth occurred at (1 0 1) face during the reaction process.

Figure 1b shows the XRD pattern of CdS sample. The peaks at 2θ = 23.56°, 30.28°, 36.44°, 43.76° and 49.32° and 61.74° correspond to (100), (101), (102), (110), (103) and (104) planes of wurtzite hexagonal CdS, respectively [24]. In the case of MnS/CdS composites, all samples present similar diffraction peaks of hexagonal CdS with lattice constants a = 0.421 nm and c = 0.647 nm, respectively. The main peak of MnS is slightly seen in the composites; either CdS peak overlaps it or its amount is comparatively less. Whatsoever, the presences of these characteristic peaks refer to the preparation MnS/CdS composites. The average crystallite size from the most intense peaks was calculated using the Scherrer Eq. 2 as given below:

$$d = \frac{B\lambda}{\beta_{1/2}\cos\emptyset} \qquad (2)$$

where d is the average crystallite size, B is the Scherrer constant (0.91), k is the wavelength of the X-ray, $\beta_{1/2}$ is full width at half maximum of the diffraction peak, and $\emptyset$ is the angle. The calculated particle size of MnS, CdS, MC1, MC2 and MC3 was 28.61, 29.54, 29.60, 29.63 and 29.78 nm, respectively.

SEM analysis

The morphology of MnS, CdS and MnS/CdS (MC1) samples at different magnifications is provided in Fig. 2. Erratically distributed spherical morphology of pure MnS nanoparticles can be seen (Fig. 2a). Higher aggregation rates were observed in this sample (Fig. 2a, a1), which were closely packed and agglomerated during the synthesis. The diameters of MnS nanoparticles are approx. 500–700 nm (Fig. 2a, a1).

Figure 2b, b1 shows SEM results of the CdS nanoparticles; urchin-like agglomerates can be seen there. Furthermore, the specific surface area of MC1 sample was studied by N_2 adsorption–desorption analysis. Type-IV isotherm with an H3 hysteresis loop indicated mesoporous structure (Fig. 2d). However, the specific surface area, pore volume and pore size are 4.95 m^2/g, 0.021 cm^3/g and 15.93 nm, respectively; thus less antibiotics adsorbed [25]. Figure 2c, c1 presents SEM images of MnS/CdS composite nanoparticles (MC1) and EDS results for target elements. The spherical MnS and spiky CdS are together in the composites (Fig. 2c) where the spiky parts of CdS are slightly reduced. As a whole, the spherical MnS and spiky CdS are in the form of composite and are urchin-like.

Figure 2 SEM images of MnS, CdS and MC1 sample (**a**, **b**, **c**) and N_2 adsorption–desorption analysis of the MC1 sample (**d**).

Raman studies

Figure 3 presents Raman spectrum of MnS, CdS and MnS/CdS composites. Peaks at 286 cm^{-1} correspond to the longitudinal optical phonon (LO) mode (A1/E1) while the peak at 583 cm^{-1} is 2 M magnon scattering [26]. As known, CdS is available in two different crystalline forms, i.e., hexagonal wurtzite and cubic zinc-blende. The wurtzite CdS presents six Raman active modes which are E_2 at 43 cm^{-1}, A_1 transverse optical (TO) at 234 cm^{-1}, E_2 at 256 cm^{-1}, E_1 (TO) at 243 cm^{-1}, A_1 longitudinal optical (LO) at 305 cm^{-1}, and E_1 (LO) at 307 cm^{-1} [27]. The peaks at 303 cm^{-1} and 601 cm^{-1} show 1LO and 2LO of active modes. MnS/CdS (MC1) sample showed three peaks at ~ 285, ~ 303, and ~ 601 cm^{-1}. Raman spectra can reflect a shift to lower or higher x-axis (broadening and downward shift) because of tensile and compressive stresses affected as reported earlier. As seen from Fig. 3b, the characteristic peaks of CdS showed blueshift in general. Compressive stresses may have caused this shift in the MC1 composite. Moreover, CdS in the MC1 sample has displayed suppressing Raman scattering band probably due to absorption of sufficient photons by CdS.

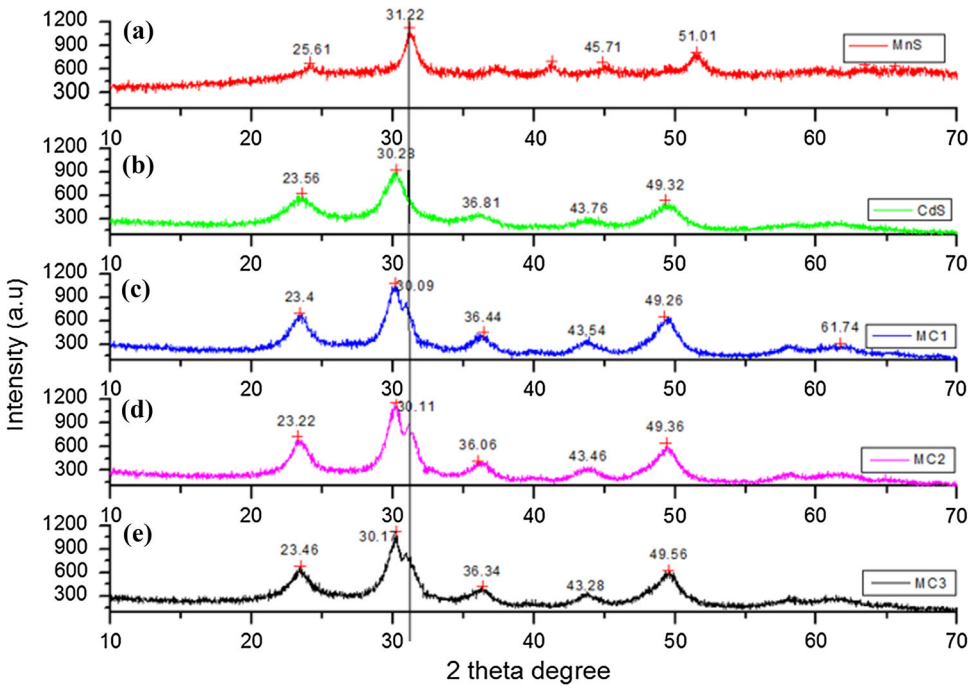

Figure 1 XRD pattern of MnS, CdS and composites (MC1, MC2, MC3).

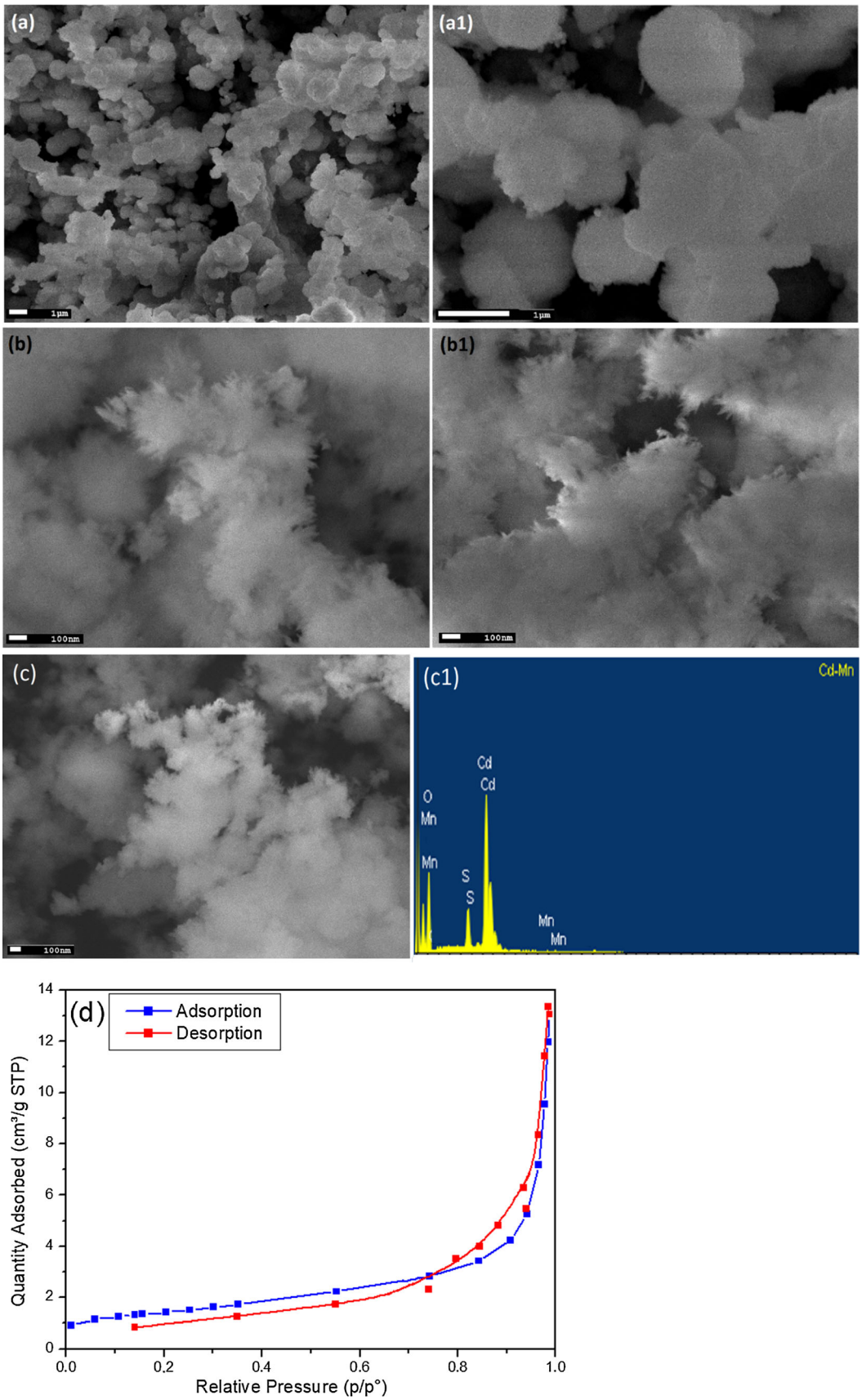
(a)
(a1)
(b)
(b1)
(c)
(c1)
Cd-Mn
Cd
Cd
O
Mn
Mn
S
S
Mn
Mn
(d)
Adsorption
Desorption
Quantity Adsorbed (cm³/g STP)
Relative Pressure (p/p°)
0
2
4
6
8
10
12
14
0.0
0.2
0.4
0.6
0.8
1.0

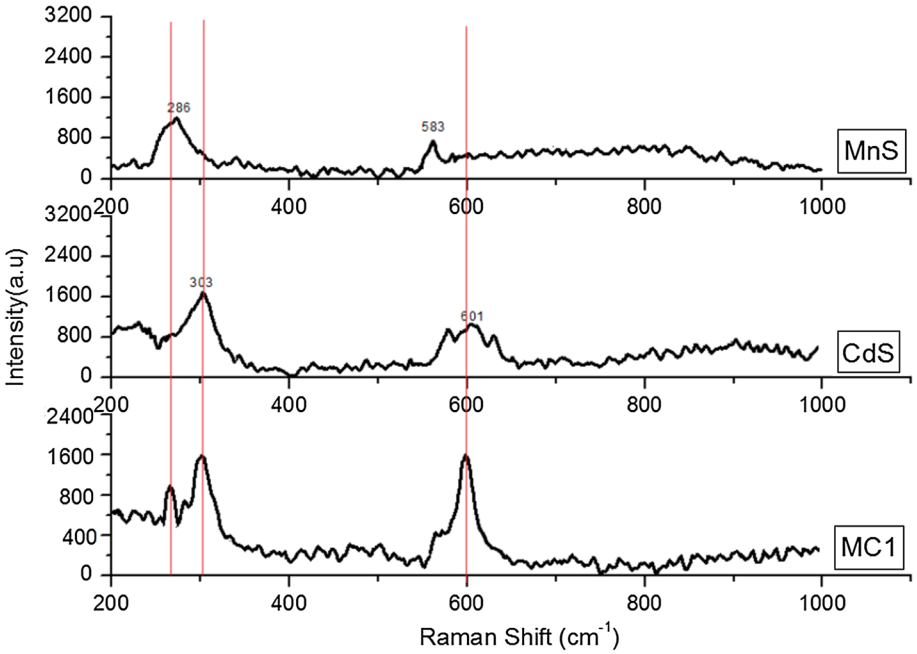

Figure 3 Raman spectra of MnS, CdS and MC1.

UV-diffuse reflectance spectroscopy (UV-DRS) Studies

Optoelectrical characteristics of the photocatalysts are obtained with UV-DRS analysis (Fig. 4). MnS presented two sharply absorption peaks at 247 and 345 nm. Probably MnS matrix gets β and γ form. Conversely, CdS displayed a visible region absorption peak at 454 nm. MC1 composite sample presented visible region absorption peaks. Surprisingly, no differences were found in the UV-DRS spectra of MC1 composite, which was highly similar to the bare CdS spectrum. A possible explanation for this might be that CdS is more dominant in terms of both electron density and crystal size.

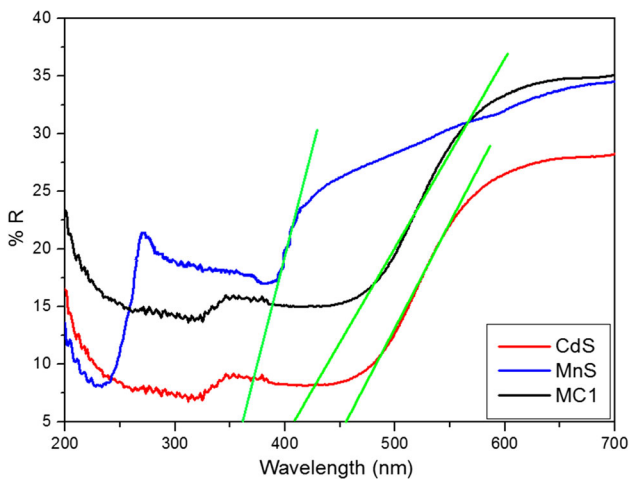

Figure 4 Diffuse reflectance spectra of MnS, CdS and MnS/CdS composites.

The band gap of each sample was calculated using Eq. 3.

$$E_g = \frac{1240}{\lambda} \tag{3}$$

where λ absorption is edge and E_g is the band gap value. A straight axis intersecting the energy showed band gap of MnS, CdS and MC1 samples as 3.31, 2.73 and 2.98, respectively. Equation 4 is used to reveal the E_{CB} and E_{VB} edge absorption.

$$E_{CB} = \delta - E_E - 0.5 \times E_g \quad \text{and} \quad E_{VB} = E_{CB} + E_g \tag{4}$$

where δ is the electronegativity of CdS (5.18 eV) [28] and E_E is the energy of free electron on the hydrogen scale (NHE, 4.5 eV). E_{CB}, E_{VB} and E_g are conduction band, valence band and bad gap values, respectively. The VB and CB values of MnS were 1.96 and − 1.34 while the VB and CB values of CdS were 2.04 and − 0.68, respectively.

Photoluminescence (PL) studies

PL is an effective study to reveal the electronic structure, photochemical and optical properties of a semiconductor. The room-temperature photoluminescence (PL) spectra (300–600 nm) of all samples are shown in Fig. 5. MnS generally excites at 270 and 300 nm. The absorption spectrum of MnS (red line

spectra) at an excitation wavelength of 300 nm consisted of three emission peaks at 425, 460 and 485 nm, respectively. The former peak at 425 nm is the near band emission of γ-MnS [29] while the last two correspond to the β-MnS of Mn^{+2} lowest energy *d–d* transitions of $^6A_1(S) \rightarrow {}^4A_1, {}^4E^4G$ and $^6A_1(S) \rightarrow {}^4T_2(^4G)$, respectively [22]. In PL of CdS (green line spectra), four emission peaks at 361, 424, 460 (purple light) and 485 nm (blue light) were observed. The peak at 485 nm can be attributed to the near band emission [30]. The emission band at 424 nm can be due to a small fraction of weakly trapped e^-/h^+ pair excitons. Moreover, due to the recombination of excitons or shallowly trapped e^-/h^+ pairs that causes band edge potential between 450 and 500 nm, the emission band was observed at 460 nm [31]. All emission peaks of pure CdS showed higher PL intensity indicating faster recombination rate of electron/hole pairs. In the case of MnS/CdS composites, introducing MnS in the MnS/CdS composite decreased the PL emission intensity. As well known, the decrease in emission intensities can be attributed to the reducing recombination of charge carriers (e^-/h^+). As seen from Fig. 5, the PL intensity of all MnS/CdS samples is lower. MC1 has presented least PL intensity but more strong separation and highest transfer efficiency of photoinduced electron/hole pairs [32]. In addition, the PL spectra of all samples have presented the combination of characteristic bands because of both MnS and CdS. This is an important issue for the future research for different photocatalyst applications.

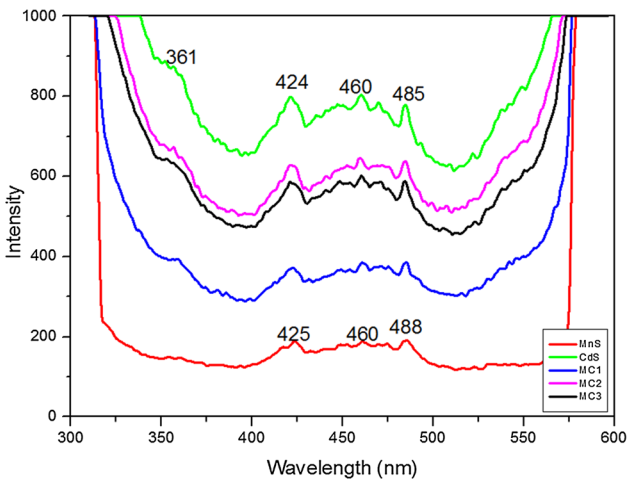

Figure 5 Photoluminescence spectra of MnS, CdS, MC1, MC2, and MC3 samples.

XPS studies

X-ray photoelectron spectroscopy (XPS) analysis was performed to reveal the chemical compositions and the surface chemical status of the MnS/CdS sample (MC1). Figure 6a shows survey spectrum of MC1 sample that clearly shows Mn, Cd and S elements. Mn 2*p* spectrum (Fig. 6b) displays two strong peaks at 641.5 eV and 652.4 eV, respectively. This energy values correspond to $2p_{1/2}$ and $2p_{3/2}$ of Mn^{2+}in MC1. As seen from Fig. 6c, two peaks, which are attributed to the Cd $3d_{5/2}$ (403.9 eV) and Cd $3d_{3/2}$ (410.1 eV), can be observed. Moreover, XPS spectra of sulfur (Fig. 6d) present two peaks at 167.23 (S $2p_{1/2}$) and 231.3 (S $2s_{1/2}$). There is a significant difference between the Cd and S binding energies. These findings suggest that there is an effective contact between MnS and CdS rather than an ordinary physical mixture. [33].

Electrochemical analysis

As is shown in Fig. 7a, Nyquist plots of MnS, CdS and MC1 composites show effective semicircles. As well known, the smaller radius confirms a faster charge transfer rate. As seen in Fig. 7a, the semicircular diameter of MC1 sample is lesser. These findings suggested that MC1 sample has excellent conductivity in the non-photo excited state [34]. This observation might support the hypothesis that there is a fast electron transfer between catalyst interfacials and also confirms the remarkably improved electron migration between the CdS and MnS interface that causes lower recombination rate of electron and hole pairs.

Dielectric results of MnS, CdS and MC1 were obtained to understand the impact of their frequency on the conductivity (Fig. 7b). Dielectric constant gives information about polarizabilities at the applied frequency [35]. The dielectric constant has decreased slowly with increasing the frequency. Dielectric constant of MC1 was higher than that of MnS and CdS probably due to the defect level, which magnified polar centers in the MC1 (MnS/CdS composite). This defect level has enhanced the photocatalytic performance of MnS/CdS (MC1) composite during the FLQ and OTC degradation.

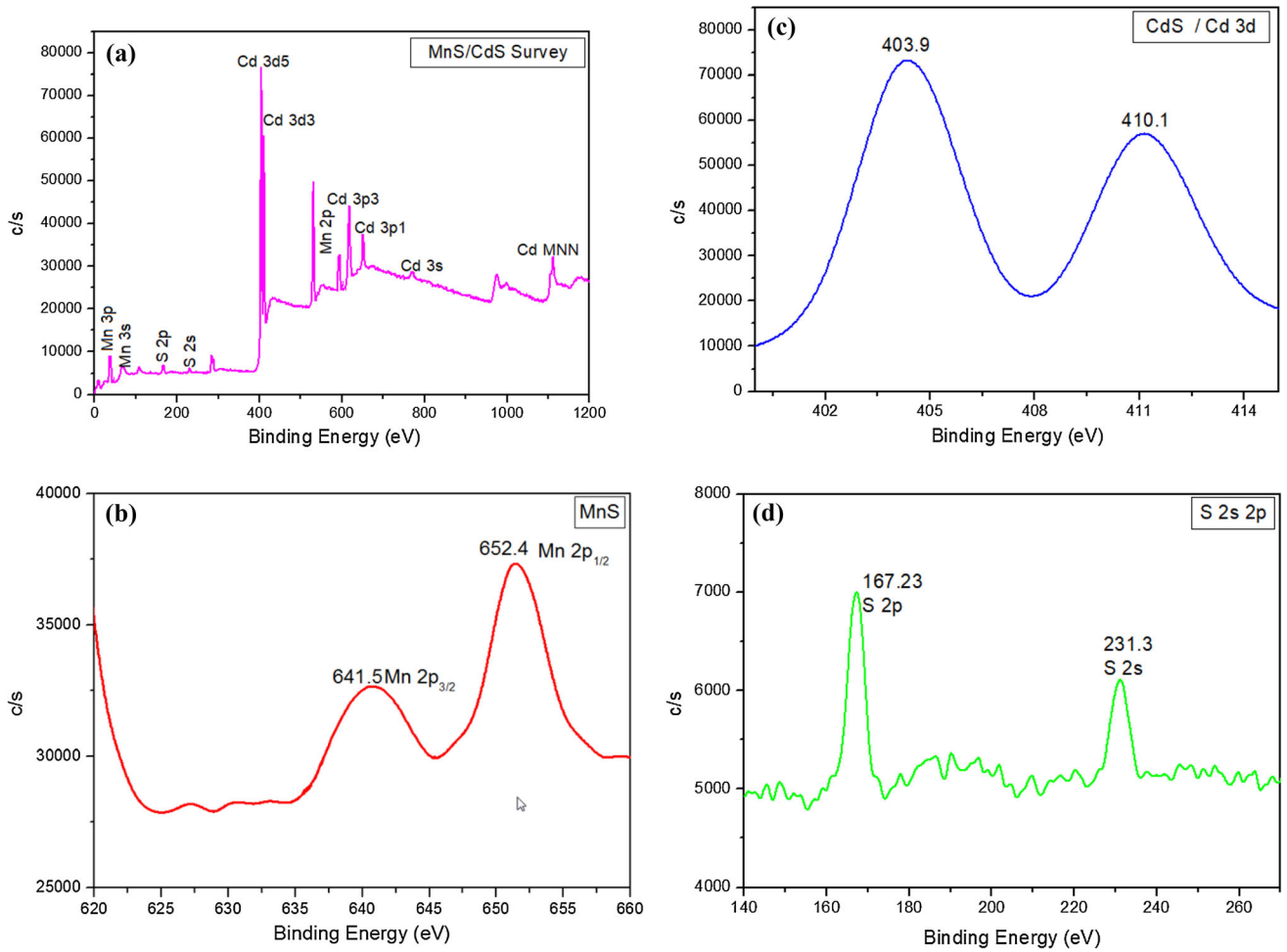

Figure 6 XPS spectra of MC1 sample **a** survey, **b** Mn 2*p*, **c** Cd 3*d*, **d** S 2*s*, 2*p*.

Photocatalytic activity

The concentration of antibiotics decreased throughout 120 min at 248 (FLQ) and 251 (OTC) nm (Figs. 8a, 9a). After 120 min of visible light irradiation, only 10% of FLQ and 11% of OTC were degraded for bare MnS, while 18% of FLQ and 19.5% of CdS were degraded for bare CdS. Comparatively, MnS/CdS composite samples showed higher photodegradation of the antibiotics under visible light irradiation (Fig. 8b, 9b). Highest degradation efficiency was reflected by MC1 composite with 83 (FLQ) and 75 (OTC) % (Fig. 8b, 9b). CdS was more reactive than MnS as the band gap of MnS is higher than the CdS. In addition, bare CdS displayed low catalytic performances because of the lower inhibition of photogenerated species and the deficiency of active sites.

Under same conditions, MnS sample showed very low degradation efficiency for both FLQ and OTC antibiotics (Fig. 8b, 9b) as MnS is not active for photocatalytic activity under visible light irradiation. The photocatalytic performance of the samples can be presented by first-order kinetic equation (Eq. 5).

$$\ln\left(C/C_0\right) = k \cdot t \tag{5}$$

where C is the concentration of antibiotics changing with time, C_0 is the initial concentration of antibiotics, k is the first-order kinetic constant, and t is the reaction time [36]. As seen from Figs. 8c and 9c, the linear correlation rate of kinetic models of the samples is very high. Moreover, the optimal CdS content (1/3.5) showed more degradation which is 11 and ~ 8 times higher than that of bare CdS for FLQ and OTC antibiotics (Fig. 8c, 9c). Further increasing the CdS loading (1/5 and 1/7 molar ratio) decreased the photocatalytic activity. It is possible that much content of CdS caused light scattering that decreased the catalyst concentration. Therefore, the reduction in

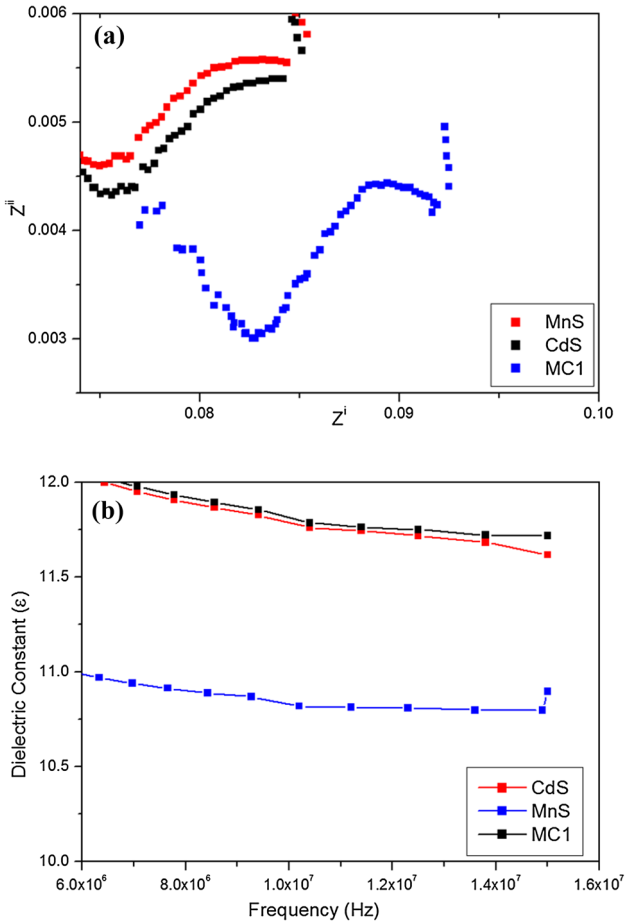

Figure 7 Electrochemical analysis of MnS, CdS and MC1 sample **a** Nyquist plots, **b** dielectric constants.

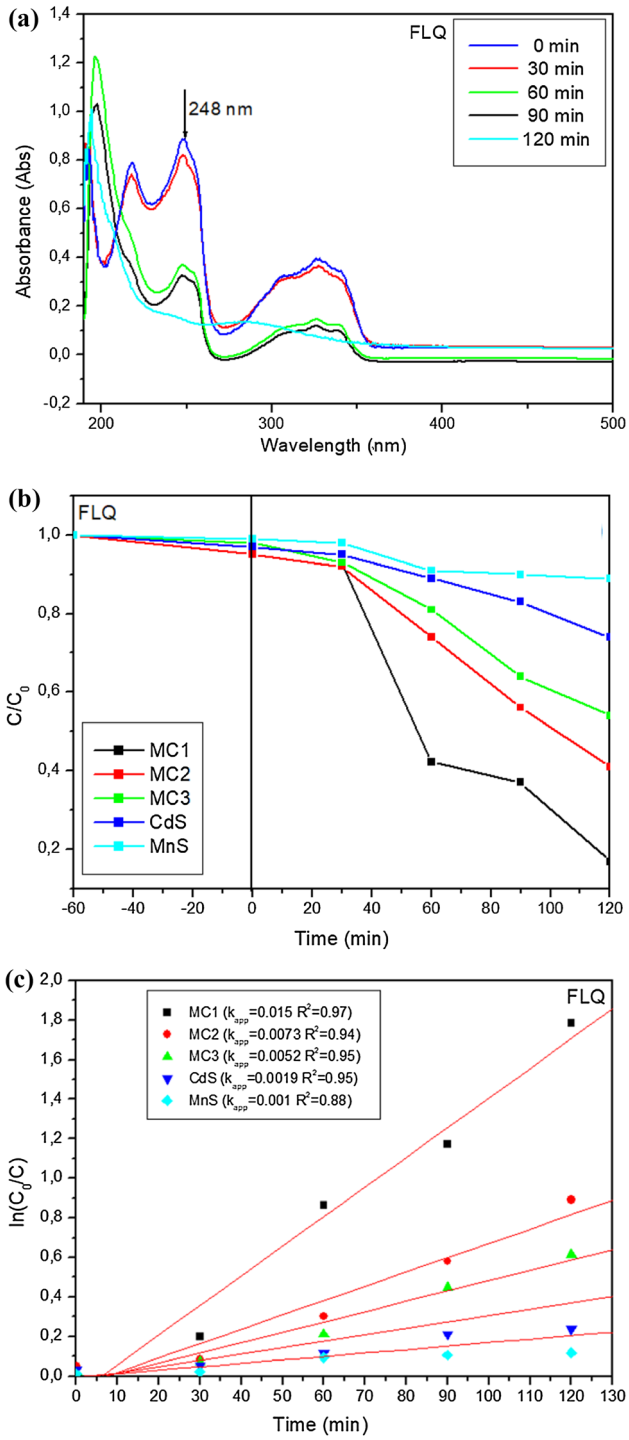

Figure 8 Photocatalytic degradation of FLQ by MC1 catalyst under visible light irradiation: **a** UV–Vis degradation profile of FLQ, **b** degradation rate and **c** pseudo-first-order kinetic results of the samples.

light intensity did not inhibit the recombination of electron ($^-$) hole (h^+) that is responsible for the degradation process.

The same MC1 composite showed higher degradation rate and where FLQ > OTC degradation. Hence, it could conceivably be hypothesized that FLQ has lower molecular weight and chemical structure; OTC is more complex and more aromatic. MC1 sample has higher degradation efficiency, although it has a broader band gap. There are two possibilities: first more defects in the crystal structure can accelerate the inhibition of electron and hole pairs; second, there is optimal content of the components in the catalyst structure. The possible charge transfer of e^-/h^+ pairs in the coupling MnS/CdS heterojunction photocatalyst could be explained as given in Fig. 10. Both CdS and MnS could be induced to reveal e^-/h^+ pairs in the CB and VB band edge, respectively. However, due to the higher band gap of MnS, the VB electrons could be excited to defect level supported with dielectric constant. Because of the intimate contact between MnS and CdS, photoinduced electrons in the CB of CdS can migrate to the

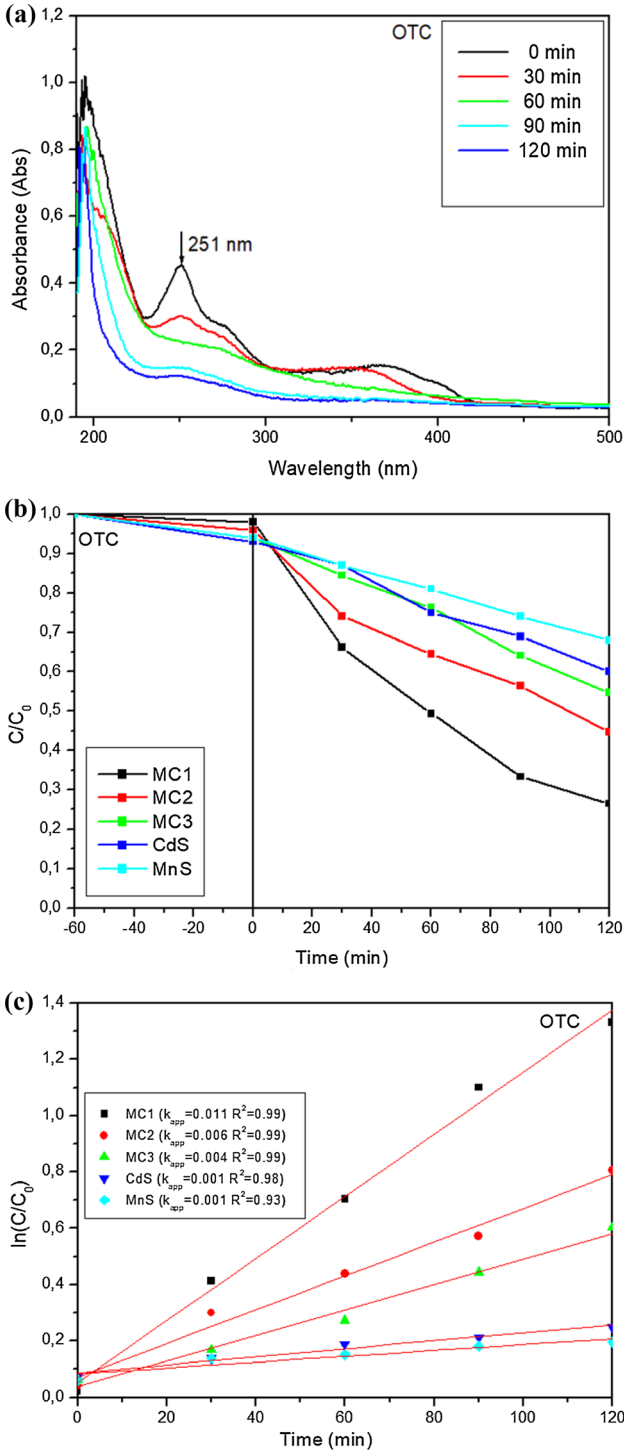

Figure 9 Photocatalytic degradation of OTC by MC1 catalyst under Visible Light irradiation: **a** UV–Vis degradation profile of FLQ, **b** degradation rate, **c** pseudo-first-order kinetic results of the samples.

defect level of MnS and also, the photogenerated holes on the VB of MnS can be transferred to the VB of CdS that would effectively separate the e^-/h^+ pairs. This formation blocks the photooxidation of CdS [37]. The redox potential of superoxide radical is − 0.33 eV. The CB electrons can produce superoxide ($\cdot O_2$) radicals with O_2 as it is more negative than the potential of $O_2/\cdot O_2$. However, VB potential of MnS and CdS is more negative than the standard redox potential of $OH^-/\cdot OH$ (2.40 eV). The transferred holes (h^+) from VB level of MnS could not reveal $\cdot OH$ radical. This finding is unexpected but suggests that $\cdot OH$ radicals were produced from superoxide radicals as shown in the reaction below:

$$O_2 + 2H_2O \rightarrow OH^- + H_2O_2 + \cdot OH$$

$$H_2O_2 \rightarrow 2\cdot OH$$

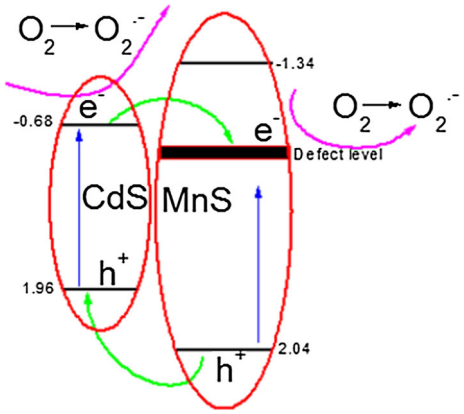

Figure 10 Charge carries distribution of MC1 composite sample for FLQ and OTC degradation under visible light irradiation.

From a different perspective, the holes might be involved in the oxidation reaction of antibiotic directly [4]. These oxidative and reductive species can cause an effective separation of charge carries indicating the higher degradation rate.

Conclusion

The MnS, CdS and MnS/CdS composites were successfully prepared via simple precipitation method. The obtained catalysts samples showed significant photocatalytic degradation and photoelectrochemical activities against FLQ and OTC. SEM images showed urchin-like composites. Although MnS has a high band gap, the CdS has shifted the composite to the visible light region. The lower peak intensity in PL spectra showed that the composite materials have effective electron/hole (e^-/h^+) inhibition. Dielectric constant data showed a possible crystalline defect in

the composite structure that has played an active role in photodegradation. MC1 (1/3.5) composite sample showed the highest degradation performance of 83 and 75% against FLQ and OTC under visible light irradiation. The photocatalytic degradation activity of the samples can be attributed to the transfer of charge carries, defect level and effective inhibition of electron/hole pairs. This study concludes the synthesis of new photocatalyst to decompose organic pollutant under visible light irradiation. More studies are required to research the commercialization of these photocatalysts.

Acknowledgement

This work was supported by Muğla Sıtkı Koçman University Coordination of Scientific Research Project Unit with 19/088/01/1/1.

References

[1] Chen X, Zhang J, Zeng J, Shi Y, Lin S, Huang G, Ji Z (2019) MnS coupled with ultrathin MoS_2 nanolayers as heterojunction photocatalyst for high photocatalytic and photoelectrochemical activities. J Alloy Compd 771:364–372

[2] Che H, Che G, Jiang E, Liu C, Dong H, Li C (2018) A novel Z-Scheme CdS/Bi_3O_4Cl heterostructure for photocatalytic degradation of antibiotics: mineralization activity, degradation pathways and mechanism insight. J Taiwan Inst Chem E 91:224–234

[3] Shao B, Liu Z, Zeng G, Wu Z, Liu Y, Cheng M, Chen M, Liu Y, Zhang W, Feng H (2018) Nitrogen-doped hollow mesoporous carbon spheres modified g-C_3N_4/Bi_2O_3 direct dual semiconductor photocatalytic system with enhanced antibiotics degradation under visible light. ACS Sustain Chem Eng. 6(12):16424–16436

[4] Shao B, Liu Z, Zeng G, Liu Y, Yang X, Zhou C, Chen M, Liu Y, Jiang Y, Yan M (2019) Immobilization of laccase on hollow mesoporous carbon nanospheres: noteworthy immobilization, excellent stability and efficacious for antibiotic contaminants removal. J Hazard 362:318–326

[5] Reyes-Garcia EA, Sun Y, Raftery D (2007) Solid-state characterization of the nuclear and electronic environments in a boron − fluoride co-doped TiO_2 visible-light photocatalyst. J Phys Chem C 111(45):17146–17154

[6] Shao B, Liu X, Liu Z, Zeng G, Zhang W, Liang Q, Liu Y, He Q, Yuan X, Wang D, Luo S (2019) Synthesis and characterization of 2D/0D g-C_3N_4/CdS-nitrogen doped hollow carbon spheres (NHCs) composites with enhanced visible light photodegradation activity for antibiotic. Chem Eng J 374:479–493

[7] Chen X, Shen S, Guo L, Mao SS (2010) Semiconductor-based photocatalytic hydrogen generation. Chem Rev 110(11):6503–6570

[8] Klimov VI (2006) Detailed-balance power conversion limits of nanocrystal-quantum-dot solar cells in the presence of carrier multiplication. Appl Phys Lett 89(12):123118

[9] Tian J, Zhang Q, Uchaker E, Gao R, Qu X, Zhang S, Cao G (2013) Architectured ZnO photoelectrode for high efficiency quantum dot sensitized solar cells. Energy Environ Sci 6(12):3542–3547

[10] Chen X, Mao SS (2007) Titanium dioxide nanomaterials: synthesis, properties, modifications, and applications. Chem Rev 107(7):2891–2959

[11] Fujishima A, Zhang X, Tryk DA (2008) TiO_2 photocatalysis and related surface phenomena. Surf Sci Rep 63(12):515–582

[12] Wang D, Xu Z, Luo Q, Li X, An J, Yin R, Bao C (2016) Preparation and visible-light photocatalytic performances of gC_3N_4 surface hybridized with a small amount of CdS nanoparticles. J Mater Sci 51(2):893–902. https://doi.org/10.1007/s10853-015-9417-y

[13] Dan M, Zhang Q, Yu S, Prakash A, Lin Y, Zhou Y (2017) Noble-metal-free MnS/In_2S_3 composite as highly efficient visible light driven photocatalyst for H_2 production from H_2S. Appl Catal B-Environ 217:530–539

[14] Huang Y, Chen J, Zou W, Zhang L, Hu L, He M, Gu L, Deng J, Xing X (2016) TiO_2/CdS porous hollow microspheres rapidly synthesized by salt-assistant aerosol decomposition method for excellent photocatalytic hydrogen evolution performance. Dalton Trans 45(3):1160–1165

[15] Nezamzadeh-Ejhieh A, Banan Z (2012) Sunlight assisted photodecolorization of crystal violet catalyzed by CdS nanoparticles embedded on zeolite A. Desalination 284:157–166

[16] Marschall R (2014) Semiconductor composites: strategies for enhancing charge carrier separation to improve photocatalytic activity. Adv Funct Mater 24(17):2421–2440

[17] Ba Q, Jia X, Huang L, Li X, Chen W, Mao L (2019) Alloyed PdNi hollow nanoparticles as cocatalyst of CdS for improved photocatalytic activity toward hydrogen production. Int J Hydrog Energy 44(12):5872–5880

[18] Oh JY, Yu JM, Chowdhury SR, Lee TI, Misra M (2019) Significant impact of Pd nanoparticle and CdS nanolayer of Pd@CdS@ZnO core-shell nanorods on enhancing catalytic, photoelectrochemical and photocurrent generation activity. Electrochim Acta 298:694–703

[19] Yang C, Lv Y, Zhang H, Zhou X (2019) Double-shelled ZnO/TiO_2/CdS nanorod arrays for enhanced photoelectrocatalytic performance. J Porous Mater 26(3):903–912

[20] Wang J, Luo J, Liu D, Chen S, Peng T (2019) One-pot solvothermal synthesis of MoS_2-modified $Mn_{0.2}Cd_{0.8}S$/MnS heterojunction photocatalysts for highly efficient visible-light-driven H2 production. Appl Catal B Environ 241:130–140

[21] Li H, Wang Z, He Y, Meng S, Xu Y, Chen S, Fu X (2019) Rational synthesis of $Mn_xCd_{1-x}S$ for enhanced photocatalytic H_2 evolution: effects of S precursors and the feed ratio of Mn/Cd on its structure and performance. J Colloid Interface Sci 535:469–480

[22] Shi Y, Xue F, Li C, Zhao Q, Qu Z (2011) Preparation and hydrothermal annealing of pure metastable β-MnS thin films by chemical bath deposition (CBD). Mater Res Bull 46(3):483–486

[23] Michel FM, Schoonen MAA, Zhang XV, Martin ST, Parise JB (2006) Hydrothermal synthesis of pure α-phase manganese (II) sulfide without the use of organic reagents. Chem Mater 18:1726–1736

[24] Channei D, Chansaenpak K, Jannoey P, Phanichphant S (2019) The staggered heterojunction of CeO_2/CdS nanocomposite for enhanced photocatalytic activity. Solid State Sci 96:105951

[25] Shao B, Liu X, Liu Z, Zeng G, Liang Q, Liang C, Cheng Y, Zhang W, Liu Y, Gong S (2019) A novel double Z-scheme photocatalyst $Ag_3PO_4/Bi_2S_3/Bi_2O_3$ with enhanced visible-light photocatalytic performance for antibiotic degradation. Chem Eng J 368:730–745

[26] Dhandayuthapani T, Girish M, Sivakumar R, Sanjeeviraja C, Gopalakrishnan R (2015) Tuning the morphology of metastable MnS films by simple chemical bath deposition technique. Appl Surf Sci 353:449–458

[27] Al-Fahdi T, Al Marzouqi F, Kuvarega AT, Mamba BB, Al Kindy SM, Kim Y, Selvaraj R (2019) Visible light active CdS@TiO_2 core-shell nanostructures for the photodegradation of chlorophenols. Photochem Photobiol A 374:75–83

[28] Channei D, Chansaenpak K, Jannoey P, Phanichphant S (2019) The staggered heterojunction of CeO_2/CdS nanocomposite for enhanced photocatalytic activity. Solid State Sci 96:105951

[29] Ren Y, Gao L, Sun J, Liu Y, Xie X (2012) Facile synthesis of gamma-MnS hierarchical nanostructures with high photoluminescence. Ceram Int 38(1):875–881

[30] Jamble SN, Ghoderao KP, Kale RB (2018) Studies on growth mechanism and physical properties of hydrothermally synthesized CdS with novel hierarchical superstructures and their photocatalytic activity. J Phys Chem Solids 114:109–120

[31] Kumar S, Ojha AK (2016) In-situ synthesis of reduced graphene oxide decorated with highly dispersed ferromagnetic CdS nanoparticles for enhanced photocatalytic activity under UV irradiation. Mater Chem Phys 171:126–136

[32] Cui H, Zhou Y, Mei J, Li Z, Xu S, Yao C (2018) Synthesis of CdS/BiOBr nanosheets composites with efficient visible-light photocatalytic activity. J Phys Chem Solids 112:80–87

[33] Fang X, Cui L, Pu T, Song J, Zhang X (2018) Core-shell CdS@MnS nanorods as highly efficient photocatalysts for visible light driven hydrogen evolution. Appl Surf Sci 457:863–869

[34] Yuvaraj S et al (2019) Hydrothermal synthesis of ZnO–CdS nanocomposites: structural, optical and electrical behavior. Ceram Int 46:391–402. https://doi.org/10.1016/j.ceramint.2019.08.274

[35] Kim YS, Tai WP, Shu SJ (2005) Effect of preheating temperature on structural and optical properties of ZnO thin films by sol–gel process. Thin Solid Films 491(1–2):153–160

[36] Vaizoğullar Aİ (2017) TiO_2/ZnO supported on sepiolite: preparation, structural characterization, and photocatalytic degradation of flumequine antibiotic in aqueous solution. Chem Eng Commun 204(6):689–697

[37] Xu Y, Chen Y, Fu WF (2018) Visible-light driven oxidative coupling of amines to imines with high selectivity in air over core-shell structured CdS@C_3N_4. Appl Catal B: Environ. 236:176–183